Broadband and High-Transmission Metasurface for Converting Underwater Cylindrical Waves to Plane Waves

Yi Chen and Gengkai Hu*

Key Laboratory of Dynamics and Control of Flight Vehicle, Ministry of Education, School of Aerospace Engineering, Beijing Institute of Technology, Beijing 100081, China

(Received 14 July 2019; published 21 October 2019)

Underwater acoustic plane waves are usually generated using transducer arrays with sophisticated control and synchronizing systems. Here, a subwavelength metasurface is proposed to convert incident cylindrical waves into plane waves by rectifying the local transmission phase through pentamode material design. The metasurface allows a high transmission because of the matched impedance between the pentamode material and water. It is also broadband since only the static material property is used in the design. A metasurface with graded unit cells is fabricated and tested in a two-dimensional water waveguide using transient cylindrical wave excitation. The experiment shows that the metasurface can convert cylindrical waves to plane waves over a broad frequency band of 15–23 kHz with an energy converting ratio as high as 69%. The working frequency band and converting efficiency can be further enhanced with smaller cells and a larger lateral size of the metasurface. This research may lead to new applications for controlling low-frequency waterborne sound, such as acoustic surveying, locating, as well as plane-wave generation for underwater acoustic-testing systems.

DOI: 10.1103/PhysRevApplied.12.044046

I. INTRODUCTION

As the only long-distance transmitted wave in water, waterborne sound is of great importance for many underwater advanced technologies, such as acoustic surveying, locating, navigation and many others. In practice, plane waves are highly demanded for long-distance transmission and underwater acoustic-testing systems, due to their directed and efficient energy transmission properties. Otherwise, the multipath interference induced by reflections at the ocean floor or free water surfaces may bring a significant challenge to decoding received signals [1]. Plane waves may be produced using transducers with comparable size to wavelength; however, this method suffers from an unacceptable large size of transducer required for low-frequency sound. A more practical technique is to explore the use of transducer arrays with controlled phase delays [2]. This requires multiple transducers and sophisticated synchronization systems and is not cost efficient. In the last decade, the development of subwavelength metamaterials significantly improves our capability of controlling wave trajectory [3,4]. The metasurface can be considered as a planar version of three-dimensional bulk metamaterials, and is more promising for practical applications owing to its compacted size [5–7]. The concept of a metasurface can be traced back to the phased array radar, where the emitted radio waves were precisely controlled by designing the phase delay of each small antenna [8]. The metasurface also relies on rectifying the phase delay of transmitted or reflected waves locally [5,6], while the phase control is achieved by the varying material properties. Many exotic functions have been demonstrated with metasurfaces, such as anomalous refraction or reflection, wave-front transformation, high-resolution imaging, orbital angular momentum generation, mathematical operation execution, thin cloaking and so on [9–19]. An excellent review on recent advances of the metasurface can be found in Ref. [20].

For waterborne sound, cylindrical waves can be produced more easily using a cylindrical transducer without size limit. Therefore, we will develop a broadband converter using the concept of the metasurface to transform incidental cylindrical waves into plane ones through local phase control. For electromagnetic waves and airborne sound, the required phase delay from 0 to 2π can be achieved with resonant mechanisms [5,6]. Such designs are, however, limited to narrow frequency bands, and suffer from a low energy conversion due to impedance mismatch. To circumvent these difficulties, designs based on bianisotropy or Willis coupling of metamaterials have been introduced, which provide a new controlling degree of freedom for the transmission phase and amplitude, simultaneously [21–25]. This concept has been demonstrated by the deflection of sound in air through a metasurface, and a rather high energy transmission is achieved [26]. However, this design concept cannot be easily generalized to waterborne sound due to the much larger impedance of

*hugeng@bit.edu.cn

water than air. Recently, solid pentamode (PM) materials have offered a new class of acoustic metamaterials with the advantages of broadband efficiency and the matched impedance with fluids [27–29]. They are designed particularly as solid structures with extremely small shear rigidity, functioning as acoustic fluids [29–32]. Through careful microstructure design, PM materials are able to achieve a high refractive index and matched impedance to water simultaneously. They are also broadband, particularly for low frequencies, since only the static material property is used. These are key ingredients for designing a broadband and high-transmission metasurface. In addition, the achievable high anisotropy in PM materials is of particular importance to bend acoustic waves for novel underwater applications, including negative refraction, planar lens, invisible cloaking and so on [32–48].

In this paper, we will design a broadband and high-transmission metasurface for converting cylindrical underwater acoustic waves into plane waves. Firstly, the design procedure for the necessary profile of a graded refractive index and the microstructure realizations is explained in detail. Then, the designed metasurface is fabricated and experimentally tested in a two-dimensional (2D) underwater waveguide to validate the design. It is observed that the metasurface can efficiently convert the incident cylindrical waves into plane waves, and an average energy converting ratio as high as 69% is achieved over a broad frequency band of 15–23 kHz, as predicted.

II. DESIGN OF PENTAMODE METASURFACE

Figure 1 shows the design procedure of the metasurface based on PM materials. As shown in Fig. 1(a), the metasurface in front of a cylindrical source is supposed to convert the incident cylindrical wave into a plane one. The required phase compensation at different locations of the metasurface can be designed according to Huygens' principle [44] [Fig. 1(b)]. The transmitted wave through the metasurface at different locations must share the same phase, and then the required phase accumulation $\phi(x)$ at different locations reads as

$$\phi(x) + k_0\sqrt{d^2 + x^2} = k_0 S_0, \tag{1}$$

where k_0 is the wave number of background water and S_0 is a constant distance. The required phase compensation is achieved by a refractive index $n(x)$, $\phi(x) = n(x)k_0 h$ with h denoting the thickness of the metasurface. The refractive index is then derived as

$$n(x) = \xi h^{-1}(S_0 - \sqrt{d^2 + x^2}). \tag{2}$$

It is noted that a scaling parameter ξ is used here to scale the refection index, and $\xi = 1$ means no scaling. By choosing an appropriate value for ξ, the required index at different locations can all be realized with the following adopted pentamode cell. Assuming the pentamode material is impedance-matched to water, the density is obtained as

$$\rho(x) = n(x)\rho_0. \tag{3}$$

In the following design, the specific parameters include the metasurface length $L = 400$ mm, the metasurface thickness $h = 55$ mm, the source distance $d = 330$ mm, the constant distance $S_0 = 7.353\ h$, and the scaling parameter $\xi = 0.93$. The required refractive index profile Eq. (2) is obviously frequency independent; therefore, the design principle works over a broadband frequency range if the material design following is also broadband. In the design of a metasurface, the thickness should, ideally, be extremely small or smaller than the operating wavelength. From Eq. (2), a smaller thickness of the metasurface h will result in a larger variation of refractive index and bring a greater challenge to the microstructure design and fabrication. Therefore, a specific thickness $h = 55$ mm is chosen here to be compatible with the proposed pentamode microstructure and the fabrication tolerance, and the thickness to wavelength ratio is approximately 0.57.

The microstructure design process of the PM materials consists of three steps, as shown in Figs. 1(c)–1(e). The rectangular metasurface of length 400 mm and thickness 55 mm is firstly divided into 23 material layers. Then, each layer is discretized into 2×7 hexagons with length 5 mm [Fig. 1(d)]. The hexagon discretization is necessary for implementing the material with real microstructure. Secondly, the required material properties for the 23 material layers are obtained from Eqs. (2) and (3) as indicated by the red line [Fig. 1(e)]. The material parameters of each layer are further realized with a hexagonal honeycomb pentamode unit cell [32] [Fig. 1(e)]. The reason for choosing a hexagonal shape and the detailed parameter design will be introduced below. Finally, pentamode cells are integrated into the corresponding hexagons in Fig. 1(c) to obtain a microstructure metasurface. The designed metasurface is then fabricated using an electric discharging machining technique, with length 400 mm, thickness 55 mm and depth 50 mm.

The main idea of the microstructure design is to make solids mimic acoustic fluids with specific index and density, or equivalently bulk modulus and density. Conventional acoustic fluids can be regarded as elastic solids with finite bulk modulus but vanishing shear modulus. Therefore, the designed solid with microstructures should have extremely small effective shear modulus, or its magnitude should be much smaller than the effective bulk modulus. These particular materials are called pentamode materials by Milton [27]. Among various beam lattices, the hexagonal honeycomb lattice meets the above requirement when

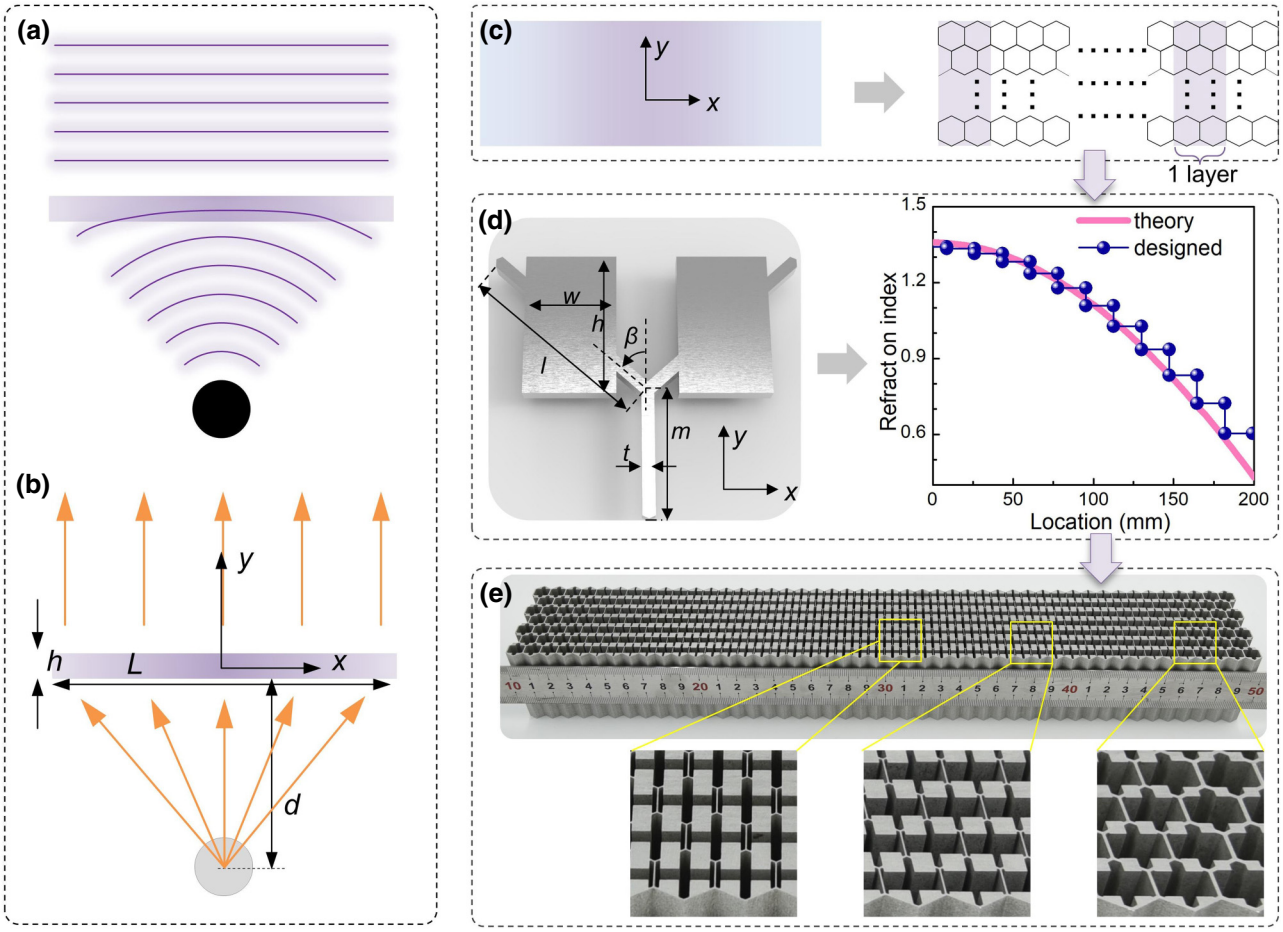

FIG. 1 Design of the pentamode metasurface. (a) Demonstration of the conversion of cylindrical waves into plane waves with a metasurface. (b) Derivation of the refractive index based on Huygens' principle. (c) The rectangular metasurface is divided into discrete hexagons. (d) The derived refractive index along the horizontal direction is approximated using layered pentamode unit cells by designing their microstructures; one half of the index distribution is shown here. The solid matrix is aluminum of Young's modulus $E_{\mathrm{Al}} = 69$ GPa, Poisson's ratio $\nu_{\mathrm{Al}} = 0.33$ and density $\rho_{\mathrm{Al}} = 2700$ kg/m^3. (e) The designed unit cells are integrated into a pentamode metasurface, and the metasurface is fabricated using an electric discharging machining technique. Inset figures show the detail.

the beams are very thin. Therefore, the hexagonal beam lattice is chosen here as a basic unit cell, and two rectangular blocks are additionally introduced into the unit cell to tune the effective density. The proposed pentamode unit cell has five nondimensional geometrical parameters (m/l, β, t/l, w/l, h/l). We first fix two parameters $m/l = 1$ and $\beta = \pi/3$ so that the hexagonal cell has an isotropic acoustic property, and tune the other three parameters (t/l, w/l, h/l) in the design. It should be noted here that these three parameters are not uniquely determined by two target values, i.e. the effective bulk modulus and density. In general, the effective bulk modulus is determined mainly by the beam thickness t/l, while the effective density is determined by w/l and h/l. A numerical optimization algorithm is used to tune the three parameters (t/l, w/l, h/l) for the required effective bulk modulus and density [32]. The solid matrix is aluminum of Young's modulus $E_{\mathrm{Al}} = 69$ GPa, Poisson's ratio $\nu_{\mathrm{Al}} = 0.33$ and density $\rho_{\mathrm{Al}} = 2700$ kg/m^3.

Figure 1(d) shows that the designed stepwise refractive index is a good approximation of the ideal distribution. The geometric parameters and effective properties of the designed pentamode cells are listed in Table I. The beam length $l = m = 5$ mm is already determined in the discretization. The effective shear modulus is nearly 2 orders of magnitude smaller than the bulk modulus, which indicates that the pentamode cells can be effectively regarded as isotropic acoustic fluids. The designed refractive index deviates from the theoretical profile by less than 5%, while the impedance is almost the same as water. The impedance-matched design is a decisive factor for the high converting efficiency of the designed metasurface. As explained above, the beams of the pentamode unit cells at

TABLE I. Geometric parameters and effective properties of each PM layer.

No.	t/l	w/l	h/l	ρ^{eff}/ρ_0	K^{eff}/K_0	G^{eff}/G_0	Z^{eff}/Z_0	n^{eff}(desi.)	n(theo.)
1	0.050	0.650	0.715	1.342	0.741	0.003	0.997	1.346	1.356
2	0.050	0.650	0.712	1.335	0.741	0.003	0.995	1.342	1.356
3	0.050	0.650	0.700	1.315	0.741	0.003	0.987	1.332	1.341
4	0.053	0.650	0.679	1.282	0.774	0.003	0.996	1.287	1.311
5	0.053	0.683	0.624	1.236	0.797	0.003	0.992	1.246	1.266
6	0.055	0.683	0.590	1.178	0.832	0.004	0.990	1.190	1.207
7	0.058	0.717	0.526	1.108	0.896	0.004	0.996	1.113	1.134
8	0.061	0.753	0.461	1.027	0.966	0.005	0.996	1.031	1.048
9	0.064	0.790	0.396	0.936	1.043	0.006	0.988	0.947	0.949
10	0.072	0.810	0.336	0.834	1.165	0.009	0.986	0.846	0.837
11	0.102	0.567	0.349	0.723	1.328	0.023	0.980	0.738	0.714
12	0.135	0.483	0.265	0.603	1.624	0.051	0.990	0.609	0.581

The first column indicates the layer number from the middle of the metasurface. The fifth to eighth columns are the effective density, bulk modulus, shear modulus and acoustic impedance, respectively. The last two columns denote the designed and theoretical index, respectively.

the center of the metasurface are thinner in order to have a larger refractive index or smaller effective bulk modulus, and they are thicker toward both ends of the metasurface to achieve a smaller refractive index. This variation is also evidently observed from the fabricated sample Fig. 1(e).

III. NUMERICAL AND EXPERIMENT RESULTS

A numerical simulation is first performed to verify the designed metasurface. Figures 2(a)–2(d) show the calculated pressure fields with the real microstructures at four frequencies. The emitted waves from a circular source are cylindrical before impinging onto the metasurface, while they are transformed into plane waves after propagating through the metasurface. The pressure intensity in the middle is larger than the lateral end locations due to the finite length of the metasurface. Over the computed frequency range, the wavelength in the water is an order of magnitude larger than the cells, and therefore the homogenization condition holds. The calculated pressure fields for the metasurface with an effective acoustic index and impedance are shown in Figs. 2(e)–2(h), and a fairly good agreement on the pressure fields between the real microstructure and effective medium is observed.

Due to a finite depth of the designed metasurface, an experimental measurement is better conducted in a 2D underwater waveguide [Fig. 3(a)] [34,49]. This can prevent wave diffraction from the top or bottom surface of the metasurface. Here, a 2D underwater acoustic waveguide immersed in a large anechoic water pool is adopted for the measurement. The 2D waveguide consists mainly of two 10-mm-thick aluminum plates and measures 1000 mm in length and 800 mm in width. The two waveguide plates are approximately 55 mm apart for mounting the sample and sweeping the pressure field. To prevent water from entering into the cavity of the PM cells, both the top and bottom of the metasurface are sealed with a 2-mm-thick polymethyl-methacrylate plate. A customized cylindrical piezoelectric transducer with a diameter of 80 mm and a height of 180 mm is suspended at the bottom of the waveguide [Fig. 3(a)], and it can generate cylindrical waves propagating upward onto the installed metasurface. One half of the marked dashed regions [Fig. 3(a)] is scanned using a hydrophone mounted on a moving stage with 10-mm steps along both directions, and the other half is obtained through a mirror operation. The scanned area is approximately 50 mm from the metasurface, and measures 200 mm and 320 mm in the horizontal and vertical directions, respectively. In order to test the broadband efficiency of the designed metasurface, the cylindrical transducer is excited by a modulated Gaussian pulse signal $\cos(2\pi f_c t) \times \exp[-(\pi f_c t/4)^2]$ with a central frequency $f_c = 19$ kHz. The Gaussian pulse has a time duration 0.23 ms with nearly four cycles, and the Fourier-transformed halfamplitude bandwidth is approximately 8 kHz. The acoustic scanning system consists mainly of a personal computer, an arbitrary wave generator (Tektronix, AWG 5002C), a step motor, a data acquisition (DA) card (Acoustic Physics, PCI-2), a customized piezoelectric transducer with a power amplifier (C-MARK, GA500) and a hydrophone (Brüel & Kjær, Hydrophone 8103) connected to a pre-amplifier (Teledyne Reson, EC6081). During the experiment, the hydrophone is first moved to a measurement location by the step motor. Secondly, the piezoelectric transducer is excited using a Gaussian pulse signal generated by the arbitrary wave generator. Then, pressure signals are collected using the hydrophone and transmitted upward to the personal computer. The steps above are repeated until all locations have been scanned. Interested readers can refer to Ref. [49] for detail information about the waveguide and the scanning process.

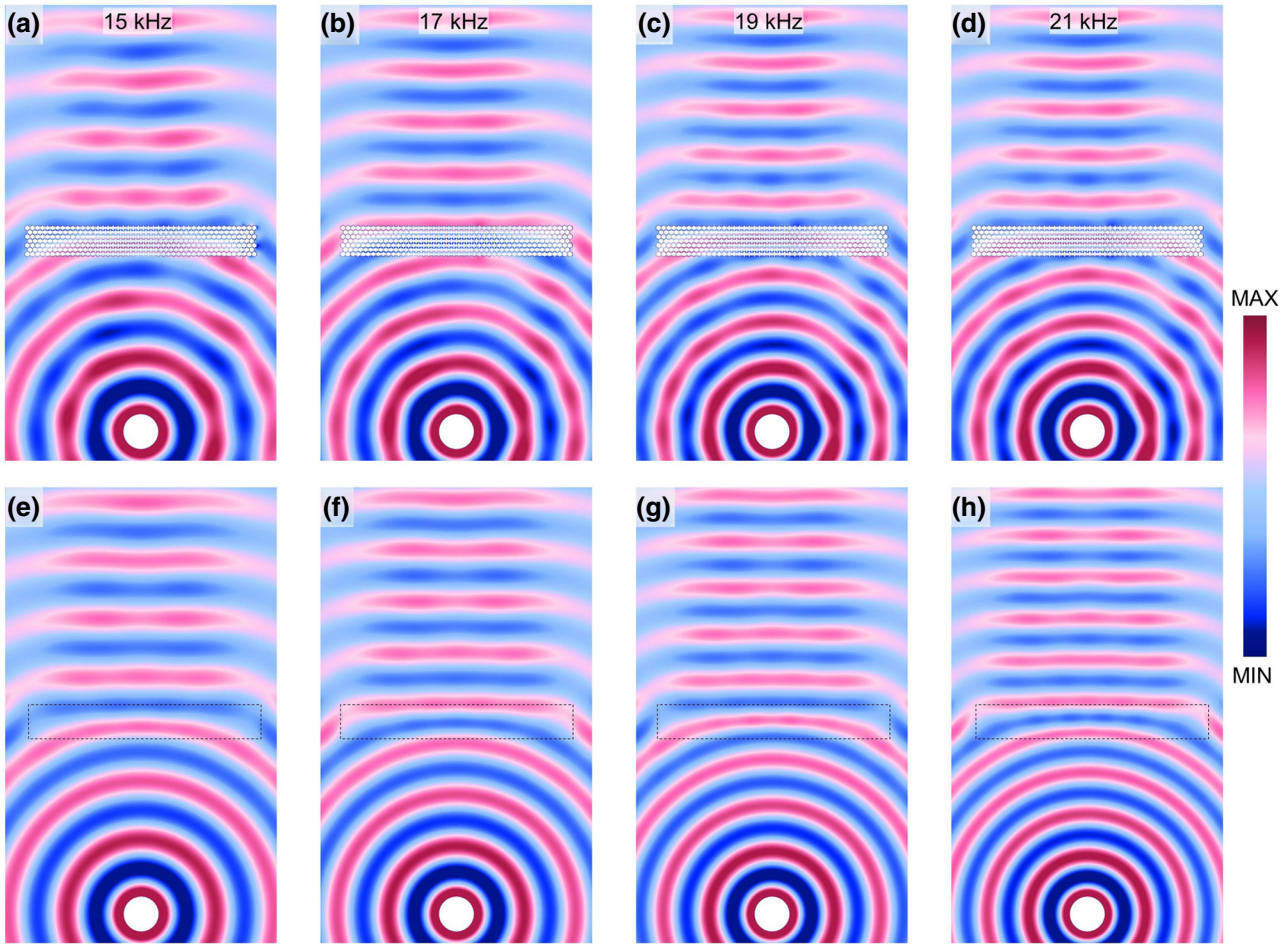

FIG. 2 Simulation of the pentamode metasurface. (a)–(d) Simulated pressure fields with microstructure metasurface corresponding to 15 kHz, 17 kHz, 19 kHz and 21 kHz, respectively. The white circle indicates the cylindrical source. (e)–(h) The same as (a)–(d) but with the metasurface replaced by a homogenized medium with an effective acoustic index and impedance. The dashed box indicates the location of the metasurface.

Figures 4(a)–4(f) show the measured instant pressure fields without and with the metasurface in the waveguide. An animation is available in the Supplemental Material showing the evolution of the wave fields [50]. In an empty waveguide [Figs. 4(a)–4(c)], a cylindrical wave propagates upward, and the pressure amplitude decays quickly during propagation due to spreading. However, using the metasurface in the waveguide designed to modify local transmission phases [Figs. 4(d)–4(f)], the transmitted wave now shows a plane-wave pattern, as predicted. In addition, the pressure-amplitude attenuation is much slower during propagation due to the high directivity of the plane wave. In accordance with the simulation results, the pressure intensity close to the lateral edges of the scanned region is weaker than in the middle. Figures 4(g) and 4(h) plot the acquired pressure signals for two marked positions at the bottom of the scanned region. A mismatch in peak time is clearly observed between the two signals for the empty waveguide, which indicates a phase delay caused by different propagating distances from the source. However, with the presence of the metasurface, the two signals are synchronized in time while having slightly different amplitudes in accordance with the reasons explained above.

To quantify the efficiency of the designed metasurface for different frequencies, we perform Fourier transformation on the measured time-domain results to obtain the pressure and phase. It is noted here that the frequency-domain results can also be directly measured using a continuous harmonic signal to excite the transducer. However, the frequency-domain experiment requires multiple measurements with different frequencies. The transient experiment performed here is more efficient since only a single measurement is required. Furthermore, the transient experiment avoids reflections from the pool boundary and the resonance of the waveguide. Figures 5(a) and 5(b) show the pressure and phase in an empty waveguide corresponding to 19 kHz where the cylindrical wave is clearly observed, particularly from the concentric phase pattern [Fig. 5(b)]. The wave pattern has a plane-wave front with

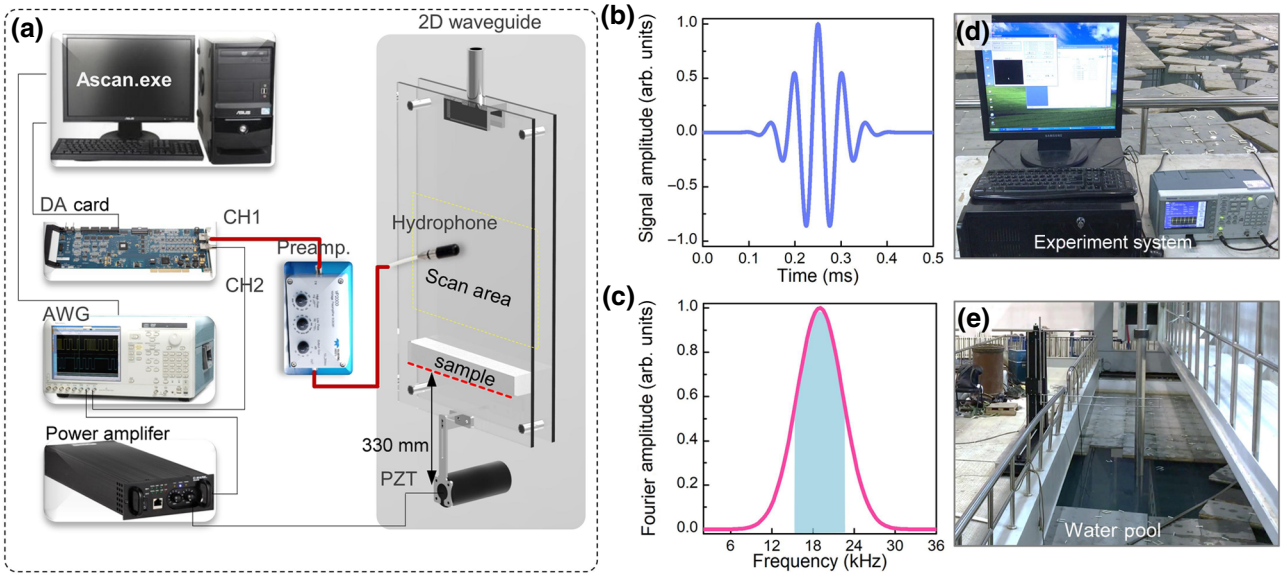

FIG. 3 Experiment setup. (a) Sketch of the acoustic measurement system and two-dimensional underwater waveguide with two aluminum plates. The two waveguide plates are rendered transparent for an interior view. (b) Time-domain plot of the Gaussian pulse with a time duration of approximately 0.23 ms used to excite the transducer. (c) Fourier-transformed amplitude of the Gaussian pulse. The central frequency is 19 kHz and the halfamplitude bandwidth is 8 kHz. (d),(e) Photograph of the experiment system and water pool.

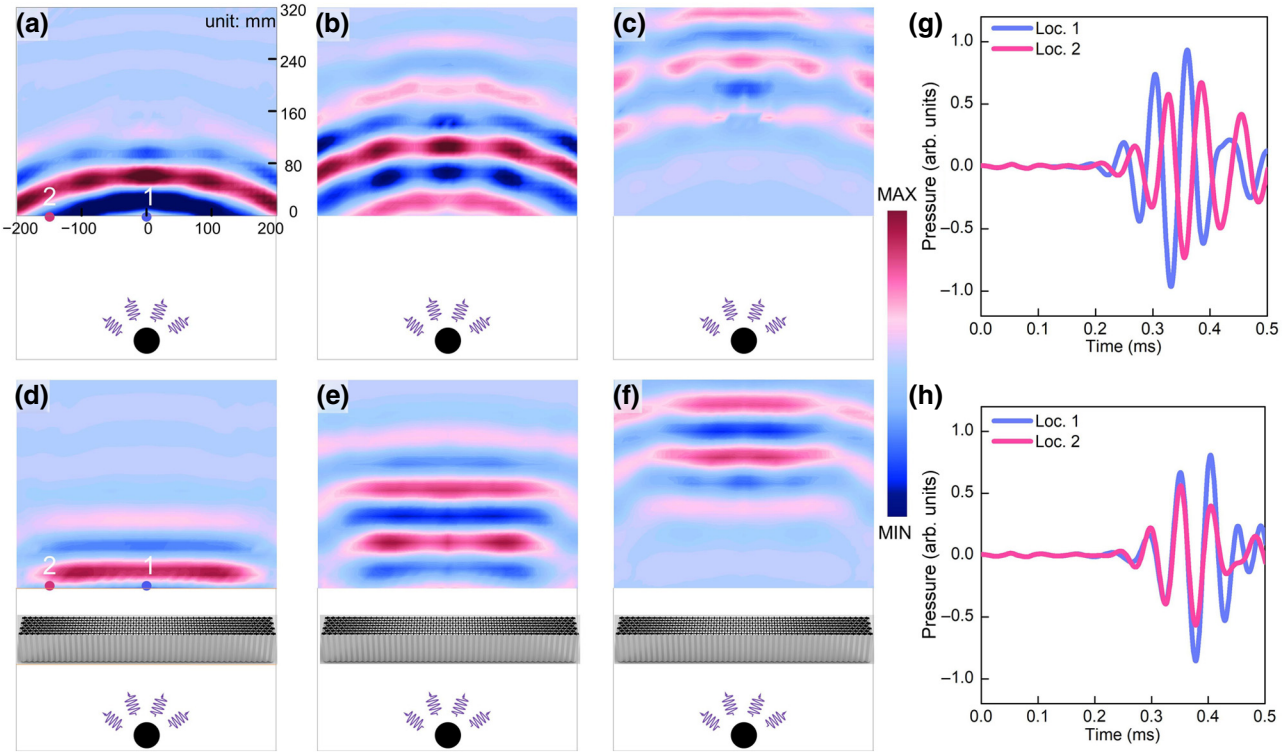

FIG. 4 Measured time-domain results. (a)–(c) Pressures fields in an empty waveguide at three different times. (d)–(e) The same as (a)–(c) but with the designed metasurface in the waveguide. (g) Pressure signals for the marked positions 1 and 2 at the bottom of the scan region in (b); position 1 lies in the center, and position 2 is 150 mm apart from position 1. (h) The same as in (g) but with the metasurface in the waveguide.

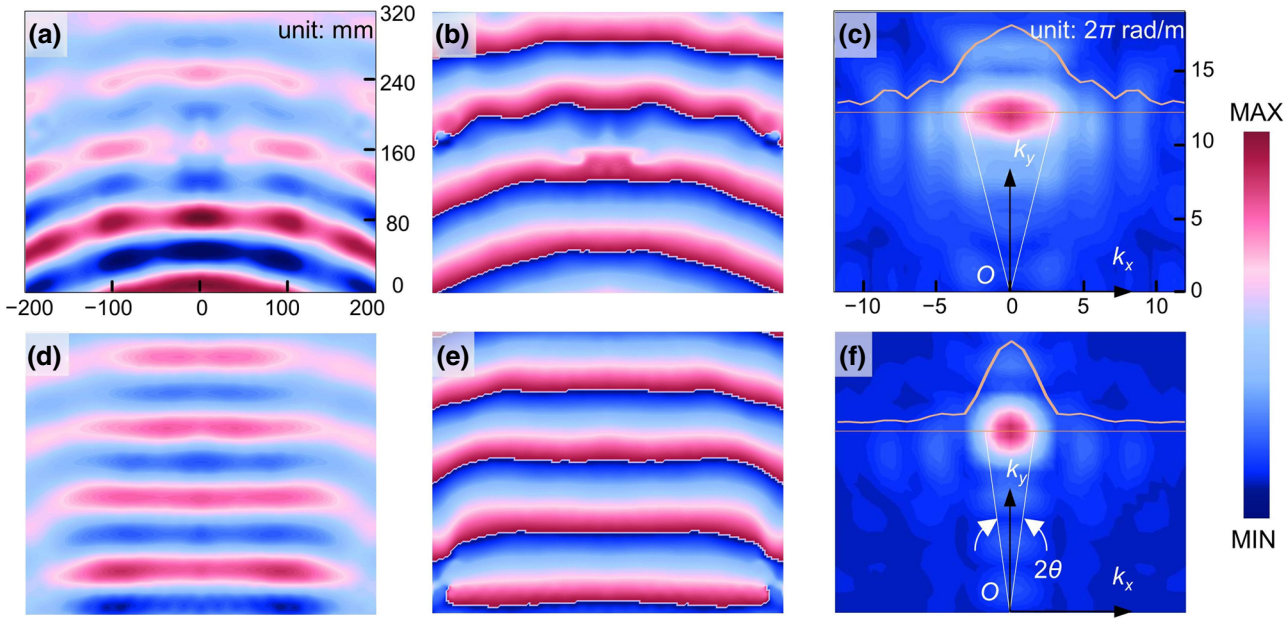

FIG. 5 Fourier-transformation results from time-domain measurements. (a),(b) Fourier-transformed pressure and phase corresponding to 19 kHz without the metasurface; further spatial Fourier transformation is performed on the pressure field in (a) to obtain the pressure amplitude in wave-vector space (c). *O* represents origin of the wave-vector space. (d)–(f) The same as in (a)–(c) but with the metasurface.

the pentamode metasurface in the waveguide [Figs. 5(d) and 5(e)]. To check the directivity of the pressure field in Figs. 5(a) and 5(d), we perform a spatial Fourier transformation to obtain the pressure amplitude in wave-vector space [Figs. 5(c) and 5(d)]. The inset curves plot the amplitude along the marked horizontal line. The spatial Fourier transformation can identify the contained wave vectors. It is observed that the measured wave field in an empty waveguide is composed of a wider range of wave vectors, while the transmitted wave through the metasurface is more localized in wave-vector space. We define an opening angle of 2θ, the half amplitude angle to the origin, to measure the directivity quantitatively. The half opening angle of θ is decreased significantly by the metasurface from 8.5° to 4.4°.

The directivity angles for the pressure field without and with the metasurface are plotted in Fig. 6. The measured half opening angle in an empty waveguide is nearly independent of frequency, and it agrees quite well with the numerical simulation. The half opening angle is significantly decreased with the pentamode metasurface, and an even smaller half opening angle is observed for high frequencies. An average half opening angle of 4.7° is achieved with the metasurface, and it has been decreased

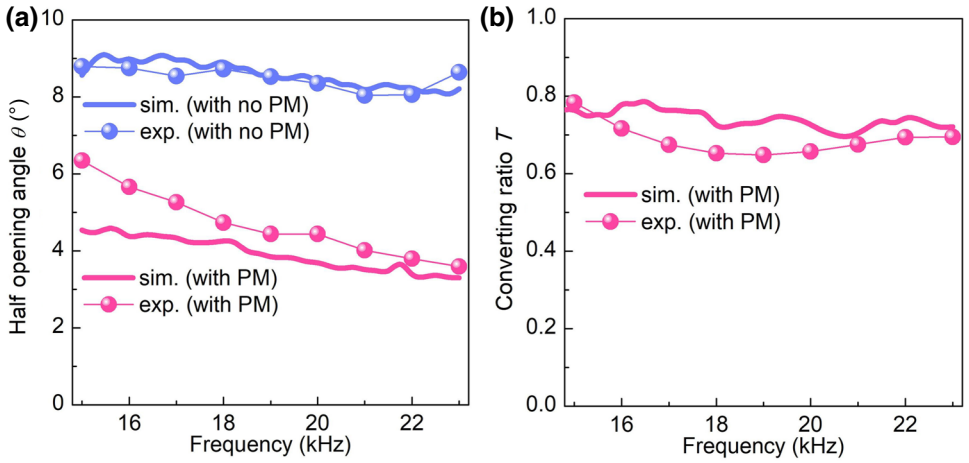

FIG. 6 Quantitative performance of the pentamode metasurface. (a) Simulated (sim.) and measured (exp.) half opening angle for measured wave field. (b) Simulated and measured energy conversion ratio.

by nearly 45% from 8.5° over the studied frequency band. Finally, we characterize the energy converting ratio of the pentamode metasurface with $T = E_T/E_I$, where E_T represents transmitted acoustic energy by the metasurface and E_I represents incident acoustic energy onto the metasurface. The acoustic energy is evaluated as an integral of energy flux $E = 1/(\rho\omega)\mathrm{Im}\int p\,\partial\bar{p}/\partial y dx$. More specifically, E_T is obtained by integrating the energy flux along the bottom of the scanned pressure fields with the metasurface, while E_I is obtained by integrating the energy flux in an empty waveguide along the red dashed line [Fig. 3(a)], which denotes the lower edge of the metasurface. The measured converting ratio is shown in Fig. 6(b) together with the simulation. In the simulation, an almost frequency-independent converting ratio of 74% is achieved, since the metasurface is designed from static effective material parameters. It should be mentioned here that, despite the fact that the pentamode metasurface is impedance-matched with water, a total transmission is not archived due mainly to two reasons. Firstly, part of the cylindrical wave is incident onto the metasurface from an oblique angle, and therefore it cannot be perfectly transmitted with only the normal matched-impedance condition. Secondly, the metasurface has a finite length, and part of the incident acoustic energy leaks out from the two side edges of the metasurface. Considering the leaked energy, the energy converting ratio of 74% is indeed quite high. In future applications, anisotropic pentamode materials can be used to achieve high transmission for arbitrary incidences as in acoustic cloaks [34]. In addition, a metasurface with a larger length and smaller thickness can also be used to suppress the energy leakage. The experiment demonstrates an average energy converting ratio of 69% over the studied frequency range of 15–23 kHz, which agrees quite well with the simulation. Due to time reversal symmetry, the metasurface can also function as a planar focusing lens for incident plane waves [36].

IV. CONCLUSIONS

In this work, a broadband and high-transmission metasurface is designed to generate plane waves from a cylindrical wave source based on the mechanism of rectifying the local transmission phase. The metasurface is made of pentamode materials with graded effective material properties. It has simultaneous broadband efficiency and high transmission. The designed metasurface is fabricated and tested under a transient cylindrical wave incidence condition in a two-dimensional underwater acoustic waveguide. It is observed that an average 69% of the energy of the incident cylindrical waves is transformed into plane waves over a broad frequency band of 15–23 kHz, and the average half opening angle is approximately 4.7°. The experiment results agree quite well with numerical simulations. In future studies, the energy converting performance can be further increased with a larger transverse dimension, a thinner thickness as well as anisotropic pentamode materials. The proposed scheme is more compact and cost effective for generating underwater plane waves than conventional transducer arrays, and may offer new opportunities for practical applications in low-frequency underwater acoustic surveying and locating.

Acknowledgments

This work was supported by the National Natural Science Foundation of China (Grants No. 11472044, No. 11632003 and No. 11802017) and the Postdoctoral Innovation Talents Support Program (Grant No. BX20180040).

[1] H. Medwin and C. S. Clay, *Fundamentals of acoustical oceanography* (Academic press, San Diego, USA, 1997).
[2] J. L. Butler and C. H. Sherman, *Transducers and arrays for underwater sound* (Springer, Cham, Switzerland, 2016).
[3] Z. Y. Liu, X. X. Zhang, Y. W. Mao, Y. Zhu, Z. Y. Yang, C. T. Chan, and P. Sheng, Locally resonant sonic materials, Science **289**, 1734 (2000).
[4] D. R. Smith, W. J. Padilla, D. C. Vier, S. C. Nemat-Nasser, and S. Schultz, Composite Medium With Simultaneously Negative Permeability and Permittivity, Phys. Rev. Lett. **84**, 18 (2000).
[5] N. Yu, P. Genevet, M. A. Kats, F. Aieta, J. Tetienne, F. Capasso, and Z. Gaburro, Light propagation with phase discontinuities: generalized laws of reflection and refraction, Science **334**, 333 (2011).
[6] X. Ni, N. K. Emani, A. V. Kildishev, A. Boltasseva, and V. M. Shalaev, Broadband light bending with plasmonic nanoantennas, Science **335**, 427 (2012).
[7] A. V. Kildishev, A. Boltasseva, and V. M. Shalaev, Planar photonics with metasurfaces, Science **339**, 6125 (2013).
[8] M. I. Skolnik, *Introduction to radar systems* (McGraw Hill Book Co., New York, 1980), pp. 590.
[9] Y. Li, X. Jiang, R. Li, B. Liang, X. Zou, L. Yin, and J. Cheng, Experimental Realization of Full Control of Reflected Waves With Subwavelength Acoustic Metasurfaces, Phys. Rev. Appl. **2**, 064002 (2014).
[10] K. Tang, C. Qiu, M. Ke, J. Lu, Y. Ye, and Z. Liu, Anomalous refraction of airborne sound through ultrathin metasurfaces, Sci. Rep. **4**, 06517 (2014).
[11] C. Pfeiffer and G. Anthony, Controlling Vector Bessel Beams with Metasurfaces, Phys. Rev. Appl. **2**, 044012 (2014).
[12] Y. Liu, Z. Liang, F. Liu, O. Diba, A. Lamb, and J. Li, Source Illusion Devices for Flexural Lamb Waves Using Elastic Metasurfaces, Phys. Rev. Lett. **119**, 034301 (2017).
[13] S. Zuo, Q. Wei, Y. Cheng, and X. Liu, Mathematical operations for acoustic signals based on layered labyrinthine metasurfaces, Appl. Phys. Lett. **110**, 011904 (2017).
[14] X. Jiang, Y. Li, B. Liang, J. C. Cheng, and L. Zhang, Convert Acoustic Resonances to Orbital Angular Momentum, Phys. Rev. Lett. **117**, 034301 (2016).

[15] B. Xie, K. Tang, H. Cheng, Z. Liu, S. Chen, and J. Tian, Coding acoustic metasurfaces, Adv. Mater., 1603507 (2016).
[16] P. Chen and A. Alù, Mantle cloaking using thin patterned metasurfaces, Phys. Rev. B **84**, 205110 (2011).
[17] Y. Li, B. Liang, Z. Gu, X. Zou, and J. Cheng, Reflected wavefront manipulation based on ultrathin planar acoustic metasurfaces, Sci. Rep. **3**, 2546 (2013).
[18] X. Ni, Z. J. Wong, M. Mrejen, Y. Wang, and X. Zhang, An ultrathin invisibility skin cloak for visible light, Science **349**, 1310 (2015).
[19] A. Silva, F. Monticone, G. Castaldi, V. Galdi, A. Al U, and N. Engheta, Performing mathematical operations with metamaterials, Science **343**, 160 (2014).
[20] B. Assouar, B. Liang, Y. Wu, Y. Li, J. Cheng, and Y. Jing, Acoustic metasurfaces, Nat. Rev. Mater **3**, 460 (2018).
[21] C. F. Sieck, A. Alù, and M. R. Haberman, Origins of Willis coupling and acoustic bianisotropy in acoustic metamaterials through source-driven homogenization, Phys. Rev. B **96**, 10 (2017).
[22] H. Nassar, Q. C. He, and N. Auffray, Willis elastodynamic homogenization theory revisited for periodic media, J. Mech. Phys. Solids **77**, 158 (2015).
[23] M. B. Muhlestein, C. F. Sieck, P. S. Wilson, and M. R. Haberman, Experimental evidence of Willis coupling in a one-dimensional effective material element, Nat. Commun. **8**, 15625 (2017).
[24] X. Su and A. N. Norris, Retrieval method for the bianisotropic polarizability tensor of Willis acoustic scatterers, Phys. Rev. B **98**, 174305 (2018).
[25] Y. Liu, Z. Liang, J. Zhu, L. Xia, O. Mondain-Monval, T. Brunet, A. Alù, and J. Li, Willis Metamaterial on a Structured Beam, Phys. Rev. X **9**, 011040 (2019).
[26] J. Li, C. Shen, A. Diaz-Rubio, S. A. Tretyakov, and S. A. Cummer, Systematic design and experimental demonstration of bianisotropic metasurfaces for scattering-free manipulation of acoustic wavefronts, Nat. Commun. **9**, 1 (2018).
[27] G. W. Milton and A. V. Cherkaev, Which elasticity tensors are realizable?, J. Eng. Mater. Technol. **117**, 4 (1995).
[28] A. N. Norris, Acoustic cloaking theory, Proc. R. Soc. A Math. Phys. Eng. Sci. **464**, 2097 (2008).
[29] A. N. Norris, Acoustic metafluids, J. Acoust. Soc. Am. **125**, 839 (2009).
[30] C. L. Scandrett, J. E. Boisvert, and T. R. Howarth, Acoustic cloaking using layered pentamode materials, J. Acoust. Soc. Am. **127**, 2856 (2010).
[31] C. N. Layman, C. J. Naify, T. P. Martin, D. C. Calvo, and G. J. Orris, Highly Anisotropic Elements for Acoustic Pentamode Applications, Phys. Rev. Lett. **111**, 2 (2013).
[32] Y. Chen, X. N. Liu, and G. K. Hu, Latticed pentamode acoustic cloak, Sci. Rep. **5**, 15745 (2015).
[33] Y. Chen, X. Liu, and G. Hu, Influences of imperfectness and inner constraints on an acoustic cloak with unideal pentamode materials, J. Sound Vib. **458**, 62 (2019).
[34] Y. Chen, M. Zheng, X. Liu, Y. Bi, Z. Sun, P. Xiang, J. Yang, and G. Hu, Broadband solid cloak for underwater acoustics, Phys. Rev. B **95**, 180104 (2017).
[35] Y. Chen, X. Liu, and G. Hu, Design of arbitrary shaped pentamode acoustic cloak based on quasi-symmetric mapping gradient algorithm, J. Acoust. Soc. Am. **140**, EL405 (2016).
[36] X. Su, A. N. Norris, C. W. Cushing, M. R. Haberman, and P. S. Wilson, Broadband focusing of underwater sound using a transparent pentamode lens, J. Acoust. Soc. Am. **141**, 6 (2017).
[37] Z. Sun, H. Jia, Y. Chen, Z. Wang, and J. Yang, Design of an underwater acoustic bend by pentamode metafluid, J. Acoust. Soc. Am. **143**, 1029 (2018).
[38] C. X. Cai, Z. H. Wang, Q. W. Li, Z. Xu, and X. G. Tian, Pentamode metamaterials with asymmetric double-cone elements, J. Phys. D Appl. Phys. **48**, 175103 (2015).
[39] M. Kadic, T. Bückmann, R. Schittny, and M. Wegener, On anisotropic versions of three-dimensional pentamode metamaterials, New J. Phys. **15**, 023029 (2013).
[40] A. Martin, M. Kadic, R. Schittny, T. Bückmann, and M. Wegener, Phonon band structures of three-dimensional pentamode metamaterials, Phys. Rev. B **86**, 15 (2012).
[41] T. Bückmann, M. Thiel, M. Kadic, R. Schittny, and M. Wegener, An elasto-mechanical unfeelability cloak made of pentamode metamaterials, Nat. Commun. **5**, 4130 (2014).
[42] R. Schittny, T. Bückmann, M. Kadic, and M. Wegener, Elastic measurements on macroscopic three-dimensional pentamode metamaterials, Appl. Phys. Lett. **103**, 23 (2013).
[43] M. Kadic, T. Bückmann, R. Schittny, P. Gumbsch, and M. Wegener, Pentamode Metamaterials with Independently Tailored Bulk Modulus and Mass Density, Phys. Rev. Appl. **2**, 5 (2014).
[44] Y. Tian, Q. Wei, Y. Cheng, Z. Xu, and X. J. Liu, Broadband manipulation of acoustic wavefronts by pentamode metasurface, Appl. Phys. Lett. **107**, 221906 (2015).
[45] A. Zhao, Z. Zhao, X. Zhang, X. Cai, L. Wang, T. Wu, and H. Chen, Design and experimental verification of a water-like pentamode material, Appl. Phys. Lett. **110**, 011907 (2017).
[46] Y. Cheng, X. Zhou, and G. Hu, Broadband dual-anisotropic solid metamaterials, Sci. Rep. **7**, 1 (2017).
[47] Z. Sun, X. Sun, H. Jia, Y. Bi, and J. Yang, Quasi-isotropic underwater acoustic carpet cloak based on latticed pentamode metafluid, Appl. Phys. Lett. **114**, 094101 (2019).
[48] R. Hedayati, S. J. Salami, Y. Li, M. Sadighi, and A. A. Zadpoor, Semianalytical Geometry-Property Relationships for Some Generalized Classes of Pentamodelike Additively Manufactured Mechanical Metamaterials, Phys. Rev. Appl. **11**, 3 (2019).
[49] M. Zheng, Y. Chen, X. Liu, and G. Hu, Two-dimensional water acoustic waveguide based on pressure compensation method, Rev. Sci. Instrum. **89**, 024902 (2018).
[50] See Supplemental Material at http://link.aps.org/supplemental/10.1103/PhysRevApplied.12.044046 for the measured pressure fields under a cylindrical wave incidence condition with and without the pentamode metasurface.